

Quasi-periodic Oscillations Associated with Spectral Branches in *RXTE* Observations of Circinus X-1

Robert E. Shirey, Hale V. Bradt, Alan M. Levine, & Edward H. Morgan

*Department of Physics and Center for Space Research,
Massachusetts Institute of Technology, Cambridge, MA 02139;
shirey@space.mit.edu*

To be published in October 10, 1998 issue of *The Astrophysical Journal* (Vol. 506)

ABSTRACT

We present *Rossi X-ray Timing Explorer* (*RXTE*) All-Sky Monitor observations of the X-ray binary Circinus X-1 which illustrate the variety of intensity profiles associated with the 16.55 d flaring cycle of the source. We also present eight observations of Cir X-1 made with the *RXTE* Proportional Counter Array over the course of a cycle wherein the average intensity of the flaring state decreased gradually over ~ 12 days. Fourier power density spectra for these observations show a narrow quasi-periodic oscillation (QPO) peak which shifts in frequency between 6.8 Hz and 32 Hz, as well as a broad QPO peak that remains roughly stationary at ~ 4 Hz. We identify these as Z-source horizontal and normal branch oscillations (HBOs/NBOs) respectively. Color-color and hardness-intensity diagrams (CDs/HIDs) show curvilinear tracks for each of the observations. The properties of the QPOs and very low frequency noise allow us to identify segments of these tracks with Z-source horizontal, normal, and flaring branches which shift location in the CDs and HIDs over the course of the 16.55 d cycle. These results contradict a previous prediction, based on the hypothesis that Cir X-1 is a high- \dot{M} atoll source, that HBOs should never occur in this source (Oosterbroek et al. 1995; van der Klis 1994).

Subject headings: Stars:individual(Cir X-1) — stars:neutron — X-rays:stars

1. Introduction

The X-ray binary Circinus X-1 is unique in its complex temporal and spectral variability. A 16.55 day cycle of flaring is observed in the X-ray (Kaluzien-ski et al. 1976) as well as optical (Moneti 1992), IR (Glass 1978), and radio bands (Whelan et al. 1977). The high degree of stability of the period of this cycle is evidence that it is the orbital period. The onset of flaring has been suggested to be the result of enhanced mass transfer occurring near periastron of a highly eccentric binary orbit (Murdin et al. 1980; Oosterbroek et al. 1995).

The X-ray profile and average intensity of the 16.55 day cycle has varied considerably over timescales of years (see e.g. Dower, Bradt, & Morgan 1982; Stewart et al. 1991; Oosterbroek et al. 1995; Shirey et al. 1996, hereafter Paper I). Observations with the *Rossi X-ray Timing Explorer* (*RXTE*) All-Sky Monitor (ASM, 2–12 keV) showed Cir X-1 in a sustained bright state with a baseline intensity level of ~ 1.0 Crab (75 c/s; 1060 μ Jy at 5.2 keV) and strong flaring up to as high as 3.5 Crab (Paper I). The flaring state began during the day following phase zero (based on the radio ephemeris of Stewart et al. 1991) and typically lasted 2–5 days (see Figure 1 and discussion below). The ratio of count rates in different ASM energy channels showed dramatic spectral softening at the onset of the flaring state and gradual hardening during the remainder of each cycle (Paper I). Similar behavior was seen in *Ginga* ASM observations folded at the 16.55 day period (Tsunemi et al. 1989). Near phase zero, some of the cycles observed with the *RXTE* ASM also showed brief dips below the 1 Crab level. Observations of dips near phase zero in Cir X-1 with *ASCA* (Brandt et al. 1996) and the *RXTE* PCA (Bradt et al. 1998) indicate the presence of both a strongly absorbed spectral component and an unabsorbed component.

Observations of type 1 X-ray bursts demonstrate that Cir X-1 is a low magnetic field neutron star (Tennant, Fabian, & Shafer 1986). Additional type 1 bursts have not been observed from Cir X-1 since the *EXOSAT* discovery, possibly because the source intensity has been higher during subsequent observations.

The rapid X-ray variability of Cir X-1 at times resembles that of both “atoll” and “Z” low-mass X-ray binaries (LMXBs) as well as black-hole candidates (Oosterbroek et al. 1995). Quasi-periodic os-

cillations (QPOs) were reported at 1.4 Hz, 5–20 Hz, and 100–200 Hz in *EXOSAT* data (Tennant 1987, 1988). Based on these data, it has been suggested that Cir X-1 is an atoll source that can uniquely reach the Eddington accretion rate and exhibit normal/flaring branch QPOs at 5–20 Hz (Oosterbroek et al. 1995; van der Klis 1994). Observations made during non-flaring phases with the *RXTE* Proportional Counter Array (PCA) showed a QPO peak that varied from 1.3 to 12 Hz, flat-topped low-frequency noise (LFN), and a broad peak that varied from 20–100 Hz (Paper I). The two QPO frequencies and the cut-off frequency of the flat-topped noise were highly correlated. These QPOs are likely to be essentially the same phenomenon as those previously seen in the *EXOSAT* observations at 5–20 Hz and 100–200 Hz.

In this paper we present additional *RXTE* ASM observations of Cir X-1 which further illustrate how its intensity profile varies from one 16.55 d cycle to another. We also present the results of *RXTE* PCA observations made over the course of one cycle in which the intensity declined unusually gradually from the flaring state to the quiescent level. This slow transition allows us to demonstrate how the time-variability properties of the source are related to its spectral properties.

2. Observations

The *RXTE* ASM has now provided 2–12 keV light curves for over 45 orbital cycles of Cir X-1 since 1996 February. Throughout all these cycles, the baseline intensity has remained near 1.0 Crab. The variety of intensity profiles is illustrated in Figure 1, which shows ASM light curves and hardness ratios for three cycles. In many cycles, after 3–5 days in the flaring state the intensity is quite steady for the remainder of the cycle (e.g., Figure 1a). In addition to the main flaring episode, some cycles show a mid-phase flare (not always at the same phase) to as high as 2 Crab (Figure 1b). Occasionally, the flaring state begins after phase zero and continues for most of the cycle with a gradually decreasing intensity (Figure 1c). All cycles observed with the ASM show the general pattern of spectral hardening mentioned above. During the half day before phase zero, and continuing intermittently for up to two days, brief dips occur in many cycles (perhaps in all cycles, since the ASM coverage is incomplete). These dips are seen as isolated low points in the ASM light curves of Figure 1.

Eight PCA observations (~ 6 ksec each) were carried out during 1997 February 18 – March 4 to sample one 16.55 day cycle at roughly two-day intervals (Figure 1c and Table 1). The very gradual decline of the flaring-state intensity in this cycle serendipitously provided an opportunity to study intensity-related source properties. All five proportional counter units (PCUs) of the PCA operated normally during each observation, except during the first few minutes of the first observation when only three PCUs were on. All intensities for that period have been adjusted by a factor of 5/3, but these data are not used in color-color and hardness-intensity diagrams due to gain differences between detectors.

Figure 2 shows the light curves and hardness ratios (with 16 s time resolution) for each of the PCA observations (I–VIII in time order), made as the intensity declined from 2.5 Crab to 1.0 Crab. On time-scales of hundreds of seconds, the observations made at high intensities show strong variability, while observations at 1.0 Crab show quite steady count rates. As expected from the ASM hardness ratios, the PCA hardness ratio gradually increases from a low value during the early observations when the source was in the flaring state to a factor four higher as it reached the quiescent level. The relationship between intensity and spectral changes is discussed in detail below.

3. Analysis and Results

3.1. Color-color and Hardness-intensity Diagrams

For the eight PCA observations of 1997 February–March, 16 s intensity and hardness-ratio measurements were used to construct color-color and hardness-intensity diagrams (CDs/HIDs, Figure 3). The hardness ratios were defined as the ratio of count rates in selected energy bands: a soft color ($I[4.8\text{--}6.3\text{ keV}] / I[2.0\text{--}4.8\text{ keV}]$) and hard color ($I[13\text{--}18\text{ keV}] / I[8.5\text{--}13\text{ keV}]$) for the CD, and a broad color ($I[6.3\text{--}13\text{ keV}] / I[2.0\text{--}6.3\text{ keV}]$) for the HID. The evolution from flaring to quiescent state produced a large range of colors and intensities over the entire cycle. In contrast, each individual observation yielded a localized cluster or track within the CDs and HIDs. The spectral branches for each of the observations are easier to distinguish in the HID than the CD. The long tracks in the HID associated with observations I–V show the color changes associated with the large intensity variations during the flaring phases. The intensity varia-

tions are smaller for observations VI–VIII, but significant color changes do occur during these observations as well.

The choice of energy bands used in constructing these diagrams can affect the appearance of spectral tracks. For observations showing a single branch, only the length and slope of the branch is affected. Observations V and VI each show two branches. The orientation of these branches is discussed in more detail below.

The tracks in the CD and HID are reminiscent of the correlated spectral/intensity behavior of Z and atoll class LMXBs, which also show correlations of temporal properties with position along tracks or branches in CDs and HIDs (Hasinger & van der Klis 1989). Thus, we have investigated how the temporal properties of Cir X-1 are related to position in the CD or HID. For this purpose, we divided the HID track for each of the eight observations into three regions (Figure 3b). The choice of numbers for each region was motivated in part by the timing results discussed below, but the numbers serve mainly as reference labels rather than as meaningful quantities (such as Z "rank number").

3.2. Power Density Spectra

Fourier power density spectra (PDSs) were computed using 16 s segments with $244\ \mu\text{s}$ (2^{-12} s) time bins. This was done for both the full 2–32 keV energy range and for four energy channels: 2.0–4.8 keV, 4.8–13 keV, 13–18 keV, and 18–32 keV. The Leahy-normalized power spectra (Leahy et al. 1983) were converted to the fractional rms normalization by dividing by the background-subtracted count rate in the selected band. The expected Poisson level, i.e. the level of white noise due to counting statistics, was estimated taking into account the effects of dead-time (Morgan, Remillard, & Greiner 1997; Zhang et al. 1995, 1996) and subtracted from each PDS; this method tends to slightly underestimate the actual Poisson level. For each of the 24 HID regions defined in Figure 3, an average PDS was calculated from the power spectra corresponding to points in that region. The PDSs were then logarithmically rebinned.

The average PDS (2–32 keV) for each HID region is shown in Figure 4. During the extended active state (observations I–VI), a broad peak is often observed near 4 Hz; this feature is prominent in PDSs from observations III–VI, weak in observation II, and

indistinguishable from a flat-topped component in observation I (see below). A strong narrow QPO feature is seen at frequencies from 6.8 to 13 Hz in observations VII and VIII. In some cases, especially at higher photon energy (see Figure 5), a harmonic peak is observed at twice the frequency of this QPO. A weak narrow QPO feature is present at frequencies above 20 Hz in regions II-1 and VI-1. A sharp “knee” is present at similar frequencies in regions II-2, II-3, III-1, IV-1, VI-2, VI-3, and possibly I-1. Broad high-frequency noise is sometimes seen, e.g. at ~ 100 Hz in observation VIII (Figure 5b). There is an underlying red continuum spectrum of noise in all of the regions of the HID, but the shape and low frequency slope of the continuum vary over a wide range.

The narrow QPO peaks and the low frequency noise in the PDSs from the “quiescent” 1 Crab observations (VII and VIII) resemble previously observed PDSs (Paper I; Oosterbroek et al. 1995; Tennant 1987). Those PDSs also contained narrow QPO features, with centroid frequencies in the range 1.3–20 Hz, and similarly shaped low-frequency noise. The broad high-frequency component that we detect in the present observations is similar to the 20–100 Hz QPO seen in earlier PCA observations (Paper I) and to the 100–200 Hz QPO observed with *EXOSAT* (Tennant 1987).

The weak narrow QPO feature above 20–30 Hz in regions II-1 and VI-1 occurs near the knee of the low-frequency noise component. This similarity to the LFN and prominent QPO at lower frequency in observations VII and VIII suggests these higher frequency oscillations are produced by the same physical process as the lower frequency QPOs. In observations II and VI, this QPO feature is visible in region 1 as a small peak that fades in region 2 and becomes only a “knee” in region 3 (see Figure 4). Thus we assume that this knee is related to the QPO. Similar knees are present in regions III-1, IV-1, and possibly I-1. We include a narrow QPO component in fits of PDSs which show a knee above 20 Hz, but identify these cases as “unpeaked” in the discussion below.

Likewise, although no peak appears in the PDSs from observation I, a broad noise component has roughly constant power below about 4 Hz and drops off above that frequency, forming a “knee” which might indicate the presence of the 4 Hz QPO component. The PDS for region I-1 somewhat resembles those of regions III-1 and IV-1, in that all show a break in the power spectrum near 4 Hz and a second

knee or change in slope near 30 Hz. We include a broad QPO component in fits of the PDSs for observation I, but we identify these cases as “unpeaked”.

The PDSs were fit with models comprising both broad-band and QPO components: a power-law for the very low frequency noise (VLFN), an exponentially cut-off power-law for the broad low-frequency noise, a Lorentzian for the broad QPO near 4 Hz, Lorentzians for the narrow QPO and its first harmonic, a broad Lorentzian for the high-frequency peak, and a second power-law to fit the residual Poisson noise at high frequency. The model for each PDS consisted of two to five of these components, depending on which components were necessary for an acceptable fit. The frequency of the harmonic (when present) of the narrow QPO was fixed at twice the fundamental frequency. For the fits of the PDSs from the four narrower energy channels, the QPO centroid frequencies were fixed at the values determined from the 2–32 keV PDSs. There were generally not enough counts to obtain useful PDS fits for the 18–32 keV channel. For use in performing the fits, we estimated the variance of each power in each binned and averaged PDS by calculating the sample variance of the powers in the individual PDSs that were averaged to obtain each point, and dividing the result by the number of the powers used in computing the sample variance.

The centroids of the narrow variable-frequency QPO and the ~ 4 Hz QPO were measured accurately whenever a clear peak was visible. However, in cases where these components are weak or unpeaked, the centroids were less well-constrained. The centroid of the broad high-frequency peak and the cut-off frequency of the LFN were often poorly constrained.

Figure 6 shows the frequency of the broad and narrow QPOs versus intensity (2–18 keV). The frequency of the narrow peak is generally correlated with intensity, starting at 6.8 Hz at 1 Crab and reaching 32 Hz at 1.3 Crab. At higher intensity, this QPO is sometimes present above 20 Hz and is often unpeaked (i.e., a knee). In observations III–VI, the broad QPO is clearly present at 3.3 to 4.3 Hz. This QPO component was included in the fits of the PDSs from observations I and II, and the resulting frequencies (2.1–4.5 Hz) are shown as unfilled squares (indicating a weak peak or a knee) above 20 kcts/s in Figure 6.

The ratio of the width of the narrow QPO peak to its centroid frequency ($\Delta\nu/\nu$) is about 0.15 when at 6.8 to 13 Hz. At higher frequency this QPO becomes

broad, with $\Delta\nu/\nu \sim 0.4$. When the broad QPO near 4 Hz is strong, we find that $\Delta\nu/\nu \sim 1$, and when it is weak $\Delta\nu/\nu \sim 2$ to 3.

Figure 7 illustrates the dependence of the rms amplitude of the QPOs upon photon energy. Typical values for the rms amplitude of the 6.8–13.1 Hz QPO at 2–4.8 keV, 4.8–13 keV, and 13–18 keV are 4%, 5%, and 8% respectively (Figure 7a), indicating a weak trend of increasing rms amplitude at higher photon energy. The amplitude of the broad QPO increases significantly at higher photon energy. For clearly peaked 4 Hz QPOs, the rms amplitude is typically about 3%, 8%, and 18% in these three energy bands (Figure 7b). The rms values vary considerably when these components are weak or unpeaked but their amplitudes still generally increase with energy (Figure 7c).

3.3. Temporal Behavior versus Position on Spectral Branches

The outlines of the HID regions of Figure 3b are reproduced in Figure 8 with labels summarizing the observed QPO properties. As the hardness ratio decreases and the intensity increases along the HID tracks for observations VIII, VII, and VI, the frequency of the narrow QPO feature increases from 6.8 Hz to 32 Hz. The feature is rather weak and knee-like in observation VI, but it appears to have a width consistent with the width of the prominent QPO peak in observations VII and VIII. A similar weak and somewhat knee-like feature is also present in observation II, where it increases in frequency from 22 Hz to 30 Hz as the intensity increases. The PDSs from observations I, III, and IV all show a knee above 30 Hz at the high-intensity, hard end of their HID tracks; these knees may be related to the narrow QPO features seen in the other observations.

The broad 4 Hz QPO is not present in the “quiescent” observations (VII and VIII). This QPO is strongest in portions of the intermediate-intensity observations (III–VI) and is weakly present in the soft, high-intensity observations (II and possibly I).

Very low frequency noise dominates the power spectrum of regions V-3 and III-3. Both of these regions appear to begin upturned branches at the low-intensity, soft end of branches showing the more pronounced 4 Hz QPOs.

4. Discussion

The combined temporal and spectral-branch properties of the observations presented here suggest Z-like behavior. We identify the 6.8–32 Hz QPOs as horizontal-branch oscillations (HBOs), the 4 Hz QPO as normal-branch oscillations (NBOs), and the strong VLFN as flaring-branch behavior (see discussion below). These identifications of characteristic time-variability patterns then help to identify the tracks in the HID as horizontal, normal, and flaring branches (HB/NB/FB), where each 6 ks observation of Cir X-1 appears to have captured a snapshot of portions of one or two of the branches. The spectral branches appear to shift around as the flaring gradually subsides, rather than forming a stable Z pattern. It is likely that the shapes of the spectral branches become distorted somewhat during these large shifts. We now describe the inferred properties of each of the spectral branches in more detail.

4.1. Horizontal Branch

HID regions VIII, VII, and VI-1 show a narrow QPO peak or knee at 6.8–7.6 Hz, 11.3–13.1 Hz, and 32 Hz respectively. This frequency range overlaps the 13–60 Hz range of typical horizontal branch QPOs (van der Klis 1995). The associated low-frequency noise and harmonic peak are also typical of horizontal branch power spectra. The broad high frequency peak in Cir X-1 may be related to the high frequency noise component often observed on the horizontal branch.

The HID track for observation VI shows the narrow QPO at 32 Hz on a roughly horizontal segment (region VI-1) and a knee at 37 Hz on the right end of this segment (region VI-2). The apex of region VI-2 brings a transition to the 4 Hz QPO, which is dominant on the downward branch of this track (region VI-3). This is very similar to the HB/NB transition in Z sources.

When Cir X-1 is in “quiescence” in observations VII and VIII, the “horizontal branch” turns upward and becomes vertical in the HID. For comparison, *RXTE* PCA observations of Cir X-1 from 1996 March 10–19 which show a narrow QPO peak at 1.3–12 Hz (Paper I) are almost entirely confined to the 12.3–14.7 kcts/s (2–21 keV) intensity range. The HID tracks for those observations lie along a nearly vertical line, and probably represent sections of the “horizontal” branch.

Observation II may also be on part of the HB, since

a weak narrow QPO appears to evolve into a knee and increase in frequency from 22 to 30 Hz as the intensity increases. However, the broad QPO is also weakly visible in PDSs for this observation. The fact that observations II, VI, VII, and VIII all show little variation of the hard color used in Figure 3a suggests that observation II may be associated with the other HB observations.

4.2. Normal Branch

The 4 Hz QPO is observed when the source intensity rises above the “quiescent” 1-Crab level (~ 13 kcts/s). It is roughly stationary in frequency (3.3–4.3 Hz when clearly peaked) and broader than the HBO. The feature is easily seen in observations III–VI; at these times the location in the HID moves along diagonal tracks. The ~ 4 Hz frequency and motion along diagonal tracks in the HID is consistent with the 4–7 Hz NBOs observed at nearly constant frequency on the NB of typical Z sources (Hasinger & van der Klis 1989). We therefore identify the broad 4 Hz QPO as a normal branch oscillation, and the diagonal tracks for observations III–VI as shifted normal branches.

The broad QPO component may be also present in the highest intensity observations, as a weak feature in observation II and in the form of a break near the 4 Hz QPO frequency in observation I. We also note that at the top of the normal branch (regions I-1, III-1, IV-1, VI-2) a knee above 30 Hz is present in addition to the NBO component.

A similar broad 4 Hz QPO is present in observations from 1996 March 5–6 made immediately before phase zero of the cycle showing the 1.3–12 Hz narrow QPO.

4.3. Flaring Branch

Beyond the left apex of the normal branch a short upturned branch is observed in HID region V-3 and possibly III-3. The PDS for these regions are dominated by very low frequency noise, which is typical for flaring branches, and no QPO peaks are obviously apparent. We note that in the well-established Z sources neither NBOs nor HBOs are present on the flaring branch, except for Sco X-1 and GX 17+2, in which the NBO evolves into a 6–20 Hz QPO (van der Klis 1995 and references therein).

The left end of the spectral track for observation V bends upward in the HID shown in Figure 3b, but bends downward in the CD in Figure 3a. This behav-

ior is demonstrated more clearly in Figure 9, which shows CDs and HIDs for observations V and VI. When a broad color ($I[6.3\text{--}13\text{ keV}] / I[2.0\text{--}6.3\text{ keV}]$) is used as the ordinate of the diagrams (Figure 9a,b), the track for observation V turns upward on the left end. When a harder color ($I[13\text{--}18\text{ keV}] / I[8.5\text{--}13\text{ keV}]$) is used as the ordinate (Figure 9c,d), this branch turns downward. The CD and particularly the HID version based on the harder color show the most clear similarity to canonical Z diagrams, with the temporal behavior of observations V and VI being generally consistent with horizontal, normal, and flaring branches. The broad-color HID (Figure 9b) shows evidence for a shift of the normal branch that does not show up in the other three diagrams of that figure.

4.4. Relation to Other Sources

Our observations reveal spectral branches which shift in the CD and HID as Cir X-1 evolves from a soft, high-intensity state to a hard, lower-intensity state. The ASM light curves and hardness ratios (Figure 1) show that this evolution occurs periodically with the 16.55 day cycle, thus suggesting that the CD/HID shifts may also be periodic. Shifts of the “Z” pattern in CDs and HIDs have been observed in the so-called Cyg-like Z sources: Cyg X-2 (Kuulkers, van der Klis, & Vaughan 1996), GX 5-1 (Kuulkers et al. 1994), and GX 340+0 (Kuulkers & van der Klis 1996). However, the shifts do not occur periodically in those sources, nor do they have the magnitude of the shifts observed in Cir X-1.

The flaring branch of Cir X-1 turns upward when a soft or broad color is used on the vertical axis. When a harder color is used, this branch turns downward but then bends to the left. In the Cyg-like Z sources, the flaring branch sometimes turns upward or starts toward higher intensity and then loops back to lower intensity (Kuulkers et al. 1996; Kuulkers et al. 1994; Kuulkers & van der Klis 1996; Penninx et al. 1991). In some cases, these sources are observed to “dip” while on the flaring branch (Kuulkers et al. 1994; Penninx et al. 1991; Wijnands & van der Klis 1997), with tracks which turn down and then to the left, similar to that of Cir X-1 in Figure 9c.

The left end of the horizontal branch in Cir X-1 turns upward and becomes vertical at low intensity (Figure 8). On this section of the branch, HBO frequencies are low: 6.8–13 Hz in observations VII and VIII and 1.3–12 Hz in the earlier 1996 March observa-

tions. A similar effect was reported in GX 5-1 (Lewin et al. 1992; Kuulkers et al. 1994), in which the HB turns upward at the low-intensity end while HBOs are observed at relatively low frequency (13–17 Hz). In fact, Lewin et al. (1992) suggested that other Z sources might show such an upward turn of the HB if their intensities and QPO frequencies became sufficiently low.

The 5–20 Hz narrow QPO was detected with *EXOSAT* at an intensity similar to the quiescent level observed by *RXTE*. We note that absorption dips are responsible for much of the structure seen in the CD shown for that observation; however, the HIDs show that the narrow QPO occurred on an upturned left end of a horizontally oriented track as in our data (see Figures 2–4, 8, & 10 in Oosterbroek et al. 1995). At higher intensity during the same observation, the narrow QPO was not present, and we note that some of the high-intensity PDSs show hints of a broad peak near 4 Hz. We thus conclude that the behavior observed by *EXOSAT* during that observation is related to the Z-like behavior we observe with *RXTE*.

Most of the other *EXOSAT* observations took place when Cir X-1 was significantly lower in intensity than the “quiescent” level of the current observations. The CDs and HIDs for these *EXOSAT* observations did not show tracks which could clearly be identified as Z or atoll. Their power spectra were generally dominated by VLFN, typical of atoll sources in the banana state, and sometimes also showed a broad red noise component resembling atoll high-frequency noise (Oosterbroek et al. 1995). However, these power-spectral shapes are not unique to atoll sources: power spectra for black hole candidates in the high state are dominated by VLFN, as are those of the current observations on the low-intensity end of the normal branch and on the flaring branch (i.e., regions III-3 and V-3).

Cir X-1 was expected to never show HBOs since atoll-like behavior was taken as evidence that the magnetic field is not strong enough to allow the magnetospheric beat frequency mechanism (MBFM) to operate (van der Klis 1994; Oosterbroek et al. 1995). (However, it is also possible that the HBOs are not produced by the MBFM.) The results presented here demonstrate both HBOs and NBOs in Cir X-1 and show no evidence for atoll behavior. Since the atoll-like behavior observed with *EXOSAT* occurred at lower intensity than in the present observations, it is possible that they do represent a different state of

the source. If Cir X-1 actually can show atoll behavior as well as the Z-like behavior shown here, then we would have new clues to the differences between the two types of sources. Such observations would challenge the hypothesis that differences in both \dot{M} and magnetic field distinguish these two classes.

5. Summary

Our results from an analysis of *RXTE* observations of Cir X-1 reveal behavior similar to that of Z sources, and, in particular, allow us to identify temporal and spectral signatures of the horizontal, normal, and flaring branches. The spectral variability of Cir X-1 is seen to correspond to tracks in a HID which are similar in direction to the typical direction in the HID of Z sources in general, but the locations of the tracks corresponding to each branch move from observation to observation in a systematic manner.

To be specific, in the current observations of Cir X-1 the horizontal branch is characterized by the presence of relatively narrow 6.8–32 Hz QPO features in the PDS. The track in the HID of the horizontal branch is horizontal at the high intensity end and becomes vertical at the low intensity end, where the source is “quiescent”, i.e., has an intensity near 1 Crab and is characterized by a relatively low degree of variability on time scales longer than 1 s. The normal branch is characterized by broad 4 Hz QPOs, and by motion in the HID which generally falls along tracks which run diagonally from hard high-intensity locations to soft low-intensity locations. There are also time intervals when the PDS is dominated by very low frequency noise. We identify these intervals as excursions onto the flaring branch.

The large amplitude intensity variations associated with the active/flaring state of Cir X-1 can be divided into three categories: (1) motion across the horizontal portion of the horizontal branch and along the normal and flaring branches, (2) shifts of the spectral branches, and (3) absorption dips. While our *RXTE* observations have allowed us to recognize and distinguish these different types of variability, there is still much to be understood about the physical mechanisms responsible.

We are grateful to the entire *RXTE* team at MIT for their support. We thank particularly R. Remillard for helpful discussions. Support for this work was provided by NASA Contract NAS5-30612.

REFERENCES

- Bradt, H., Shirey, R., & Levine, A. 1998, in Nuclear Physics B Proceedings Supplements, The Active X-ray Sky: Results from Beppo-SAX and Rossi-XTE, ed. L. Scarsi, H. Bradt, P. Giommi, & F. Fiore (Elsevier Science B. V.)
- Brandt, W. N., Fabian, A., Dotani, T., Nagase, F., Inoue, H., & Kotani, T. 1996, MNRAS, 283, 1071
- Dower, R., Bradt, H., & Morgan, E. 1982, ApJ, 261, 228
- Glass, I. S. 1978, MNRAS, 183, 335
- Hasinger, G. & van der Klis, M. 1989, A&A, 225, 79
- Kaluźienski, L. J., Holt, S. S., Boldt, E. A., & Serlemitsos, P. J. 1976, ApJ, 208, L71
- Kuulkers, E. & van der Klis, M. 1996, A&A, 314, 567
- Kuulkers, E., van der Klis, M., Oosterbroek, T., Asai, K., Dotani, T., van Paradijs, J., & Lewin, W. G. H. 1994, A&A, 289, 795
- Kuulkers, E., van der Klis, M., & Vaughan, B. A. 1996, A&A, 311, 197
- Leahy, D. A., Darbro, W., Elsner, R. F., Weisskopf, M. C., Sutherland, P. G., Kahn, S., & Grindlay, J. E. 1983, ApJ, 266, 160
- Lewin, W. H. G., Lubin, L. M., Tan, J., van der Klis, M., van Paradijs, J., Penninx, W., Dotani, T., & Mitsuda, K. 1992, MNRAS, 256, 545
- Moneti, A. 1992, A&A, 260, L7
- Morgan, E. H., Remillard, R. A., & Greiner, J. 1997, ApJ, 482, 993
- Murdin, P., Jauncy, D. L., Haynes, R. F., Nicolson, G. D., Holt, S. S., & Kaluźienski, L. J. 1980, A&A, 87, 292
- Oosterbroek, T., van der Klis, M., Kuulkers, E., van Paradijs, J., & Lewin, W. G. H. 1995, A&A, 297, 141
- Penninx, W., Lewin, W. G. H., Tan, J., Mitsuda, K., van der Klis, M., & van Paradijs, J. 1991, MNRAS, 249, 113
- Shirey, R. E., Bradt, H. V., Levine, A. M., & Morgan, E. H. 1996, ApJ, 469, L21
- Stewart, R. T., Nelson, G. J., Penninx, W., Kitamoto, S., Miyamoto, S., & Nicolson, G. D. 1991, MNRAS, 253, 212
- Tennant, A. F. 1987, MNRAS, 226, 971
- Tennant, A. F. 1988, MNRAS, 230, 403
- Tennant, A. F., Fabian, A. C., & Shafer, R. A. 1986, MNRAS, 221, 27P
- Tsunemi, H., Kitamoto, S., Manabe, M., Miyamoto, S., & Yamashita, K. 1989, PASJ, 41, 391
- van der Klis, M. 1994, ApJS, 92, 511
- van der Klis, M. 1995, in X-Ray Binaries, ed. W. G. H. Lewin, J. van Paradijs, & E. P. J. van den Heuvel (Cambridge University Press: Cambridge), 252
- Whelan, J. A. J. et al. 1977, MNRAS, 181, 259
- Wijnands, R. & van der Klis, M. 1997, in Proceedings of the 8th Annual Astrophysics Conference in Maryland, ed. S. S. Holt & T. Kallman
- Zhang, W., Jahoda, K., Swank, J. H., Morgan, E. H., & Giles, A. B. 1995, ApJ, 449, 930
- Zhang, W., Morgan, E. H., Jahoda, K., Swank, J. H., Strohmayer, T. E., Jernigan, G., & Klein, R. I. 1996, ApJ, 469, L29

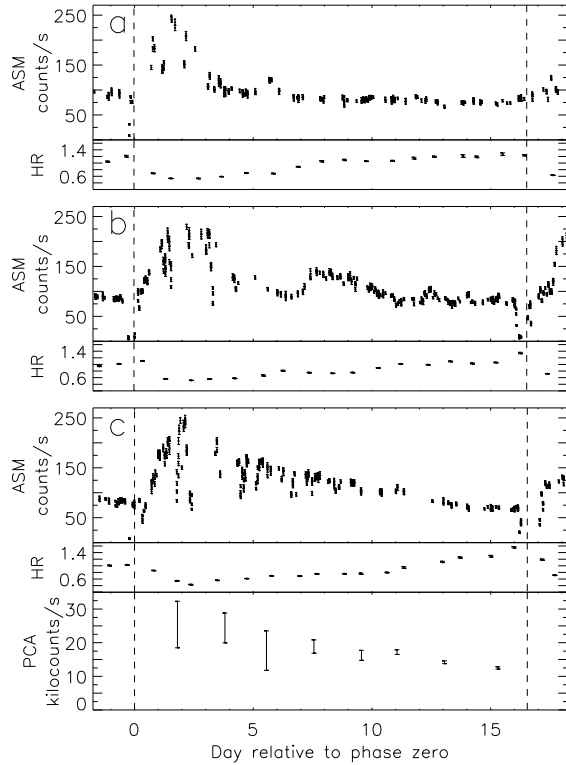


Fig. 1.— *RXTE* ASM light curves (1.5–12 keV) for three 16.55 d cycles of Cir X-1 showing different flaring profiles. Each intensity point corresponds to a 90-s exposure by one of the three ASM cameras, and the hardness ratio (HR), defined as the ratio of counting rates for 5–12 keV to 3–5 keV, is shown in one-day averages. The 3–5 keV to 1.5–3 keV hardness ratio exhibits very similar behavior and is not shown here. The intensities are for Cir X-1 after background and other sources in the field of view have been subtracted. The Crab nebula yields ~ 75 c/s. Vertical dashed lines indicate phase zero based on the radio ephemeris of Stewart et al. (1991). Day zero corresponds to (a) 1997 April 23.87 (b) 1996 August 2.14 and (c) 1997 February 16.69. For cycle (c), the intensity ranges ($I[2.0\text{--}18\text{ keV}]$) seen in the eight *RXTE* PCA observations (I–VIII in time order) are also shown.

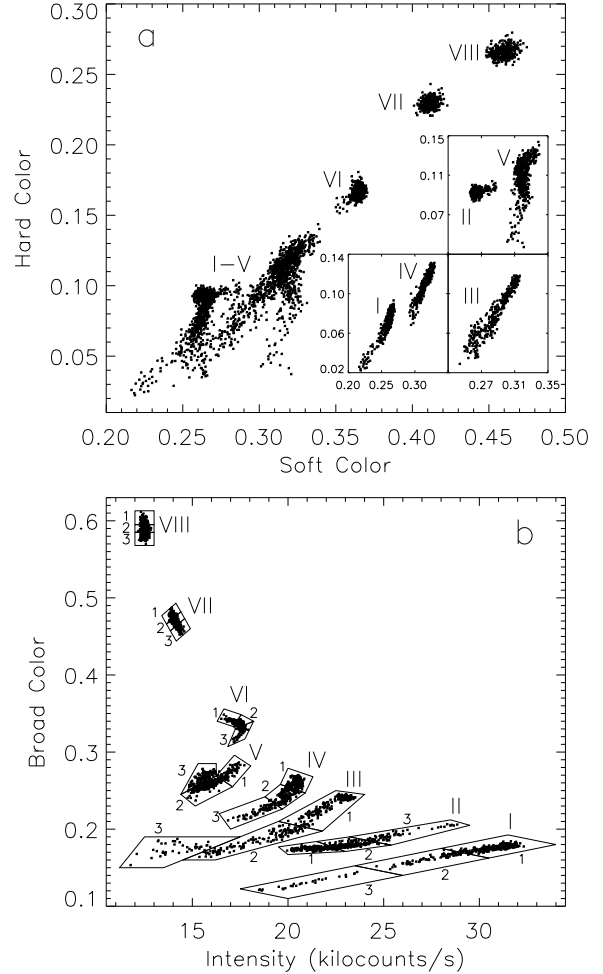


Fig. 3.— Color-color diagram (a) and hardness-intensity diagram (b) for all eight observations (I–VIII). In the CD, soft color is defined as $I[4.8\text{--}6.3\text{ keV}] / I[2.0\text{--}4.8\text{ keV}]$ and hard color as $I[13\text{--}18\text{ keV}] / I[8.5\text{--}13\text{ keV}]$. In the HID, the intensity, $I[2.0\text{--}18\text{ keV}]$, is from all five PCUs and the hardness ratio is a “broad” color: $I[6.3\text{--}13\text{ keV}] / I[2.0\text{--}6.3\text{ keV}]$. Each point corresponds to 16 s of data. Background has been subtracted, but it does not affect the intensity or soft color and only slightly affects the hard color. The three insets in the CD separate overlapping points from observations I–V. The HID track for each observation has been divided into three regions (1–3) for timing analysis.

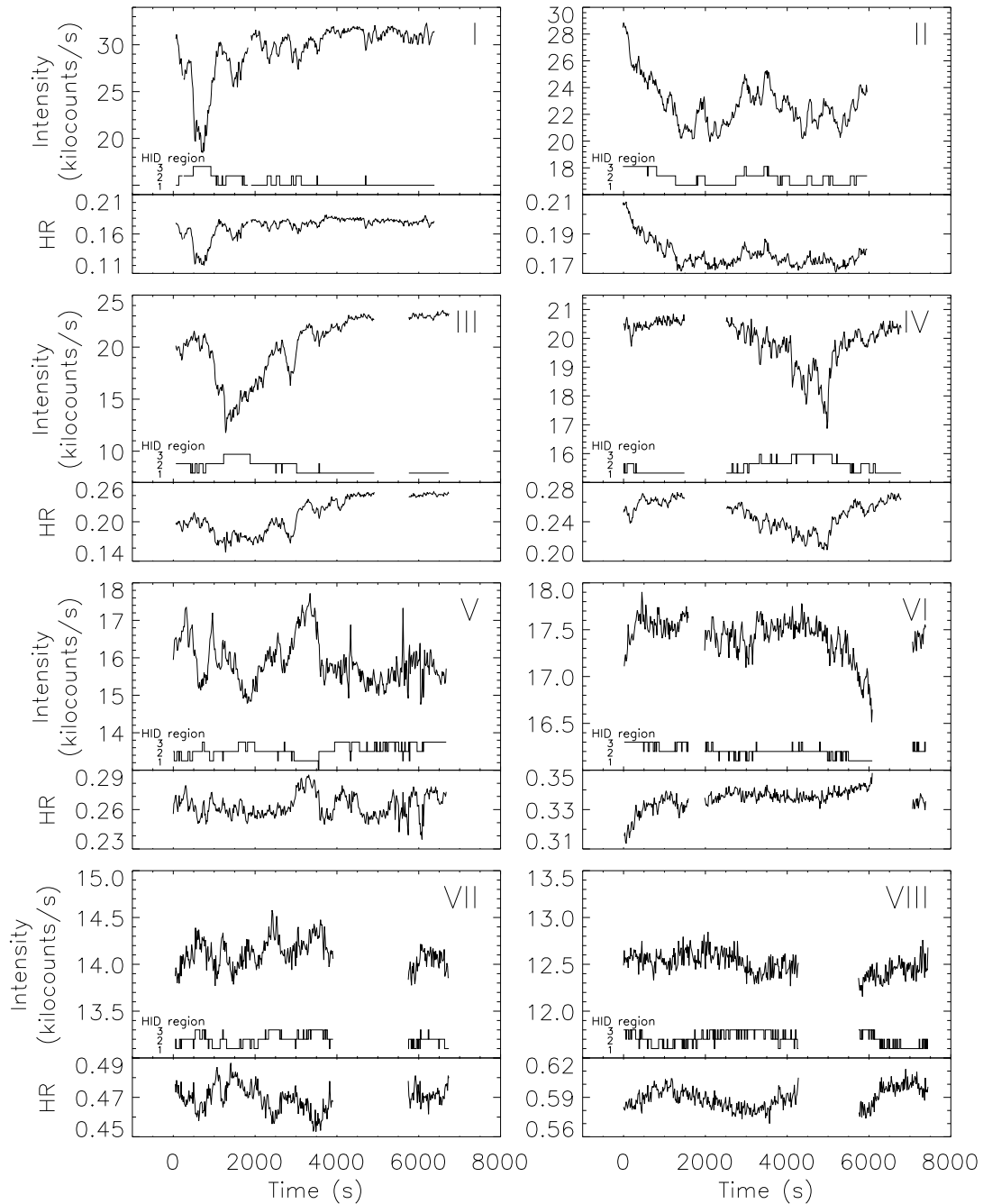


Fig. 2.— PCA light curves (2–18 keV, 5 PCUs) and hardness ratios ($HR = I[6.3\text{--}13\text{ keV}] / I[2.0\text{--}6.3\text{ keV}]$) in 16 s time bins for the eight observations made during 1997 February 18 – March 4. A count rate of 13 kcts/s \approx 1.0 Crab. The data gaps in Obs. VI were longer than as shown here; the second segment of the observation has been shifted left by 4000 s and the third segment by 5000 s. These data were used to construct the hardness-intensity diagram in Figure 3. The association with specific regions of that diagram is indicated below each light curve.

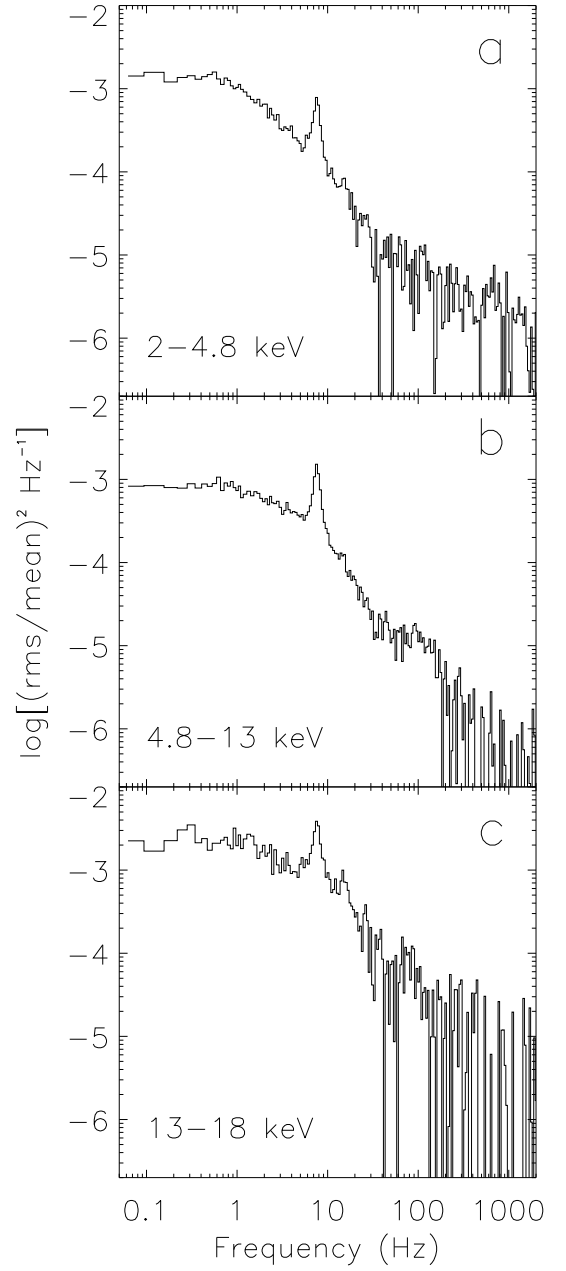
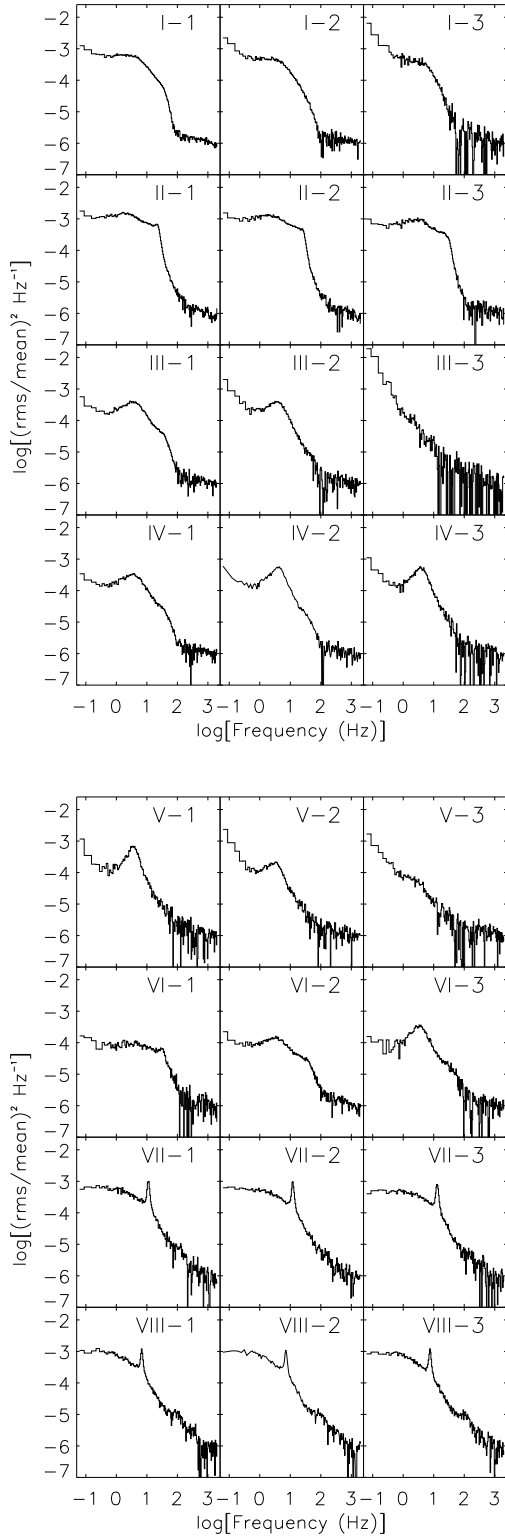


Fig. 5.— Averaged and rebinned power density spectra for HID region VIII-3 in three energy bands. A harmonic peak of the 7.6 Hz QPO is clearly visible in the high-energy channel (c). The broad high-frequency peak, most clear in (b), occurs near ~ 100 Hz in this observation. The low-frequency noise cuts off less sharply as energy increases.

Fig. 4.— Averaged and rebinned power density spectra (2–32 keV) for each of the three HID regions for each observation. Poisson noise has been subtracted from each PDS (see text).

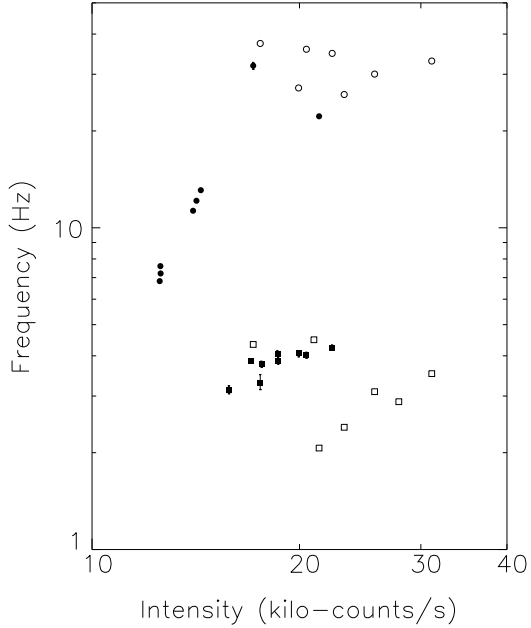


Fig. 6.— Centroid frequency of the QPOs versus intensity ($I[2.0\text{--}18\text{ keV}]$). A filled circle represents the narrow QPO and a filled square represents the broad ~ 4 Hz QPO (all points below 5 Hz are the broad QPO). Unfilled circles and squares indicate the approximate frequency of a knee or very weak peak that may be associated with the narrow and broad QPO respectively. Error bars on frequency measurements (filled points only) represent 90% confidence intervals for a single parameter ($\Delta\chi^2=2.7$). In many cases, the error bar for the QPO frequency is smaller than the plot symbol.

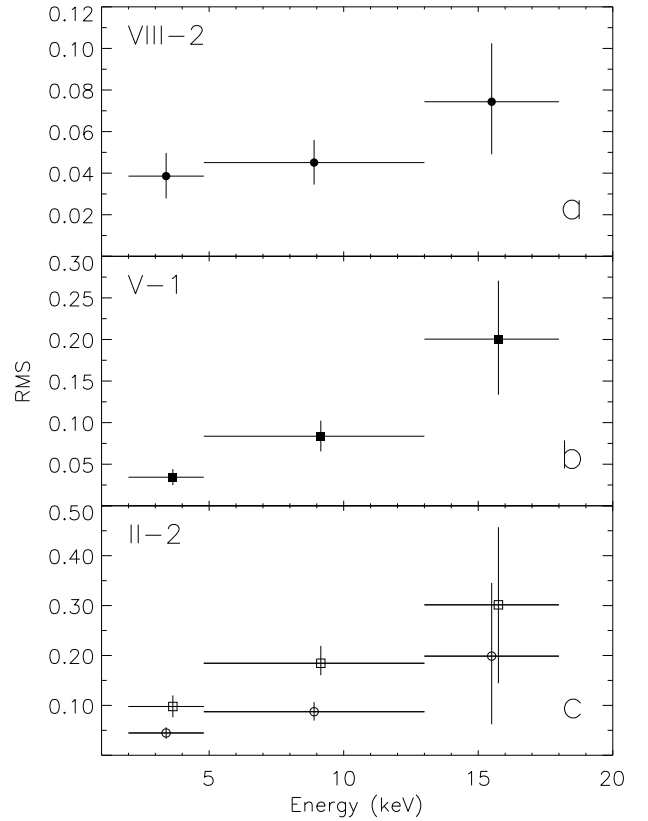


Fig. 7.— Rms amplitude of QPOs versus photon energy. Panel (a) shows the rms for the narrow QPO at 7.2 Hz (solid dot) and (b) for an example of the broad 4 Hz QPO (solid box). In panel (c), unfilled circles and boxes indicate the rms amplitude of a component forming a knee or very weak peak that may be associated with the narrow and broad QPOs respectively. The broad QPO points have been offset slightly to the right in energy for clarity. Errors on QPO amplitudes represent 90% confidence intervals.

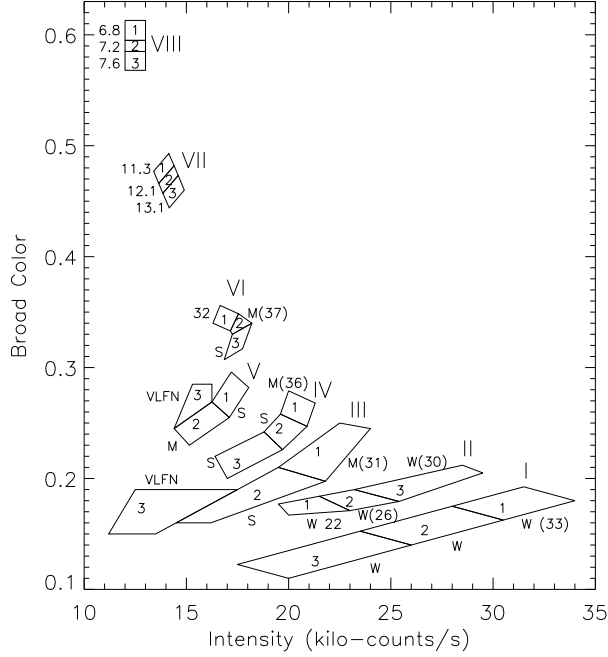


Fig. 8.— Hardness-intensity diagram showing QPO properties for the regions from Figure 3b. The frequency of the 6.8 to 32 Hz QPO is labeled (in Hz) beside each region where it is present. Parenthesized frequencies indicate that this component was unpeaked, i.e., a knee. Letters indicate the strength of the broad 4 Hz QPO: S—strong, M—medium, and W—weak or unpeaked.

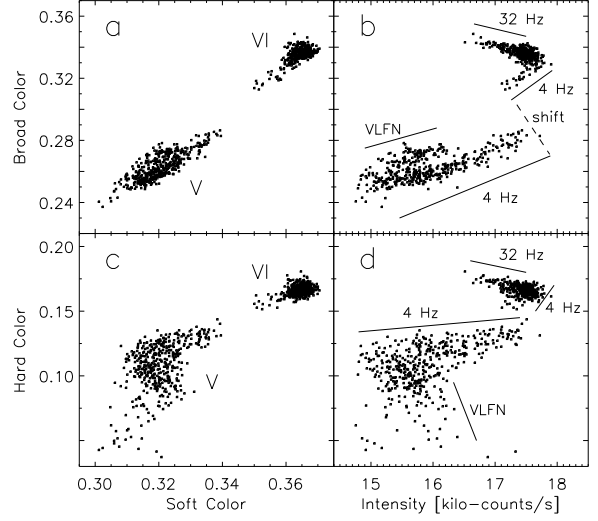


Fig. 9.— Broad-color and hard-color CDs and HIDs for observations V and VI. In all four diagrams, Obs. V is in the lower left and Obs. VI in the upper right. The CD and HID tracks for Obs. V both turn upward at the left end in the broad-color diagrams (a,b) but turn downward in the hard-color diagrams (c,d). In the HIDs, presence of the 32 Hz HBO, 4 Hz NBO, and VLFN is indicated along the branches. An apparent shift of the normal branch between observations V and VI is labeled in (b). The intensity, $I[2.0-18 \text{ keV}]$, is from all five PCUs. The soft color is defined as $I[4.8-6.3 \text{ keV}] / I[2.0-4.8 \text{ keV}]$, the broad color as $I[6.3-13 \text{ keV}] / I[2.0-6.3 \text{ keV}]$, and the hard color as $I[13-18 \text{ keV}] / I[8.5-13 \text{ keV}]$. Each point corresponds to 16 s of background-subtracted data.

TABLE 1
PCA OBSERVATIONS OF CIR X-1 DURING 1997 FEBRUARY 18 – MARCH 4

Obs.	Julian Date ^a	Phase	Mean Intensity ^b (Crab)
I	2450497.90	0.10	2.3
II	2450499.98	0.23	1.8
III	2450501.69	0.33	1.6
IV	2450503.66	0.45	1.5
V	2450505.80	0.58	1.2
VI	2450507.31	0.67	1.3
VII	2450509.35	0.79	1.1
VIII	2450511.62	0.93	1.0

^aMidpoint of 2-3 hr observation (~ 6 ksec of data per observation)

^b1.0 Crab $\approx 13,000$ counts/s (2–32 keV)